Line-profile variability in the beta Cephei star epsilon Centauri

Schrijvers, C.; Telting, J.H.; Aerts, C.

Link to publication

Line-profile variability in the β Cephei star ϵ Centauri[⋆]

C. Schrijvers[1,2], J. H. Telting[3], and C. Aerts[4]

[1] Astronomical Institute Anton Pannekoek, University of Amsterdam, and Center for High Energy Astrophysics,
Kruislaan 403, 1098 SJ Amsterdam, The Netherlands

[2] Space Department, TNO TPD, Stieltjesweg 1, 2600 AD Delft, The Netherlands
e-mail: schrijvers@tpd.tno.nl

[3] Nordic Optical Telescope, Apartado 474, 38700 Santa Cruz de La Palma, Spain

[4] Instituut voor Sterrenkunde, Katholieke Universiteit Leuven, Celestijnenlaan 200B, 3001 Leuven, Belgium
e-mail: conny@ster.kuleuven.ac.be

Abstract. We present an analysis of 530 high-resolution spectra of the β Cephei star ϵ Cen, showing complex variations in the rotationally broadened absorption line-profiles of the Si III triplet (λ 4552, 4567, 4574 Å). Most data were acquired during four dedicated observing runs between April 1996 and June 1998, with time spans between 6 and 14 days. We calculate velocity moments of the line profiles and apply Fourier analysis techniques to analyze their time behavior. The variations of the velocity moments confirm the presence of two periods already known from photometry, and provide evidence for the presence of two or more non-radial pulsation modes. Our analysis of the spectral time series concentrates on the variability at each position in the λ 4567 Å line profile. In addition to the two frequencies found in the radial-velocity variations, we find several other periodicities to be present across the line profile. We use Fourier analysis, sinusoid fitting, and folding techniques to analyze the amplitude and phase information for each of the detected periods. We find evidence for at least five pulsation modes in ϵ Cen, and identify ℓ-values between 2 and 5.

Key words. line: profiles – stars: early-type – stars: oscillations – stars: rotation – stars: variable: other – stars: individual ϵ Cen

1. Introduction

The bright early-B type star ϵ Cen (HD 118716, spectral type B1III, $m_V = 2.3$, Hoffleit & Jaschek 1982) was discovered to be a multi-periodic small-amplitude β Cephei star by Shobbrook (1972), who could identify two pulsation frequencies of 5.896 and 5.651 d^{-1} in his photometric dataset. Later, Heynderickx (1991, 1992) could only trace the first frequency in his own photometry, 5.90 d^{-1}, and additionally found a signal at frequency 5.23 d^{-1}. Heynderickx argued that the difference in the results of these works may well be due to the limited sampling of these datasets (Shobbrook and Heynderickx used 390 and 103 data points respectively).

ϵ Cen has been the subject of many investigations, some of which have revealed some of its fundamental parameters. From interferometric observations Hanbury Brown (1974) derived an angular diameter, corrected for limb darkening, of 0.48 ± 0.03 mas. Using this value together with UV, optical and IR observations, Code et al. (1976) derived an effective temperature of $T_{\rm eff} = 25\,740$ K. Somewhat cooler temperatures have been derived by De Geus et al. (1989, using Walraven photometry) $T_{\rm eff} = 23\,440$ K

and $\log g = 3.68$, Heynderickx et al. (1994, Walraven photometry) $T_{\rm eff} = 23\,930$ K and $\log g = 3.76$, North & Nicolet (1990, Geneva photometry) $T_{\rm eff} = 23\,880$ K and $\log g = 3.71$, and Balona & Shobbrook (1984, Strömgren photometry) $T_{\rm eff} = 22\,280$ K and $\log g = 3.79$.

Blaauw (1964) determined membership of the Lower-Centaurus Crux (LCC) subgroup of the Sco-Cen OB association, for which De Geus et al. (1989) derived an age of about 11×10^6 yr. Investigating the Hipparcos proper motion data, De Zeeuw et al. (1999) did not include ϵ Cen in their LCC members list. However, as Hipparcos found that the motion of the star on the sky is not compatible with that of a single star, they noted that binarity or multiplicity may have caused them to discard ϵ Cen as an LCC member.

Combining the above information with the Hipparcos parallax, $\pi = 8.7 \pm 0.8$ mas, reasonably accurate estimates for the mass, radius and maybe also the age of the star can be derived. This, together with the observed multi-periodicity, makes ϵ Cen interesting for asteroseismological research.

Brown & Verschueren (1997) determined the projected equatorial rotation velocity, $V_{\rm e} \sin i$, to be 114 ± 15 km s^{-1}. Their result is based on two different techniques; they used artificially broadened sharp-lined template spectrum matching the

Table 1. The spectra were mostly obtained during four dedicated observing runs and are supplemented by 16 spectra from intermediate periods. Columns 1 to 5 indicate observing run, time span, number of obtained spectra, number of nights in which useful data was acquired, and number of high-quality nights with a minimum of 10 spectra, respectively.

Run	Time Span [d]	# of Spectra	# of Nights	# of HiQ Nights
April 1996	5.37	74	6	4
May 1997	8.16	134	7	5
March 1998	12.30	209	10	9
June 1998	13.12	97	12	6
Other	-	16	6	0
Total	775.27	530	41	24

measured FWHM of weak metal lines, as well as a fit of the λ 4026 Å line profile with theoretical spectra.

Here we present a first attempt to derive pulsation periods of ϵ Cen from high-resolution spectroscopy. If the pulsation periods can be determined, the spectroscopic time series are likely to contain enough information to derive the pulsational ℓ values and possibly also m values (Balona 1986; Gies & Kullavanijaya 1988; Aerts et al. 1992; Telting & Schrijvers 1997). Spectroscopic observations of the line-profile variations of ϵ Cen have not been presented in the main literature before.

In Sect. 2 we will discuss the data. In Sect. 3 we present the Fourier analysis of the time series. We investigate the variability at each of the detected frequencies in Sect. 4. Our mode identification is in Sect. 5. We list our conclusions in Sect. 6.

2. Observations and reduction

The 530 high-resolution spectra ($R = 65\,000$) were obtained at ESO La Silla, with the CAT telescope equipped with the CES spectrograph, over 4 observing runs supplemented by 16 spectra from intermediate periods (see Table 1). During the first three runs, the ESO Long Camera projected a spectral range of 52.2 Å onto about 2600 useful columns of ESO CCD #38, sampling the wavelength region of the Si III triplet (λ 4552, 4567, 4574 Å). In June 1998 we used the ESO Very Long Camera giving rise to spectra of 19.5 Å, which covered only the latter two Si III lines. With the exception of a few spectra, the exposure time was kept shorter than 10 min (typically 4 min). S/N ratios of the extracted spectra are between 450 and 1200. The reduction of the spectra was performed similar to that of ω^1 Sco which were taken during the first observing run (see Telting & Schrijvers 1998). We rebinned the spectra from June 1998 to match the binning of the other spectra.

For the first three observing runs, the continuum shape is affected by vignetting of the light beam. Together with the short piece of continuum, red-wards of the λ 4574 Å line, the vignetting troubled the continuum rectification of the λ 4574 Å line profile which makes this line less useful for analysis. Because the λ 4552 Å line profile was not covered by the spectra from April 1996, the only good line profile that is present in all spectra is the λ 4567 Å line profile.

Figure 1 shows examples of the measured line-profile variations of the λ 4567 Å line profile. One can see a pattern of bumps moving from the blue to the red side of the line profiles. From the variable and sometimes asymmetric bump pattern we expect that the star is multi-periodic: two or more non-radial pulsation modes must be present. The number of bumps that seem to travel across the line profile indicates that modes of high ℓ (say $\ell \gtrsim 4$) must be present in ϵ Cen.

2.1. Variations of the equivalent width and the velocity moments

We calculate the equivalent width (EW) and the first few velocity moments of the λ 4567 Å line profile. The moments are calculated as defined in Schrijvers et al. (1997, hereafter S97), and are related to the centroid (M_1), width (M_2), and skewness (M_3) of the line profiles. We use 4567.8 Å as the rest wavelength and for the integration domain we use 4565.6–4570.3 Å.

The EW and all three velocity moments show variations. Figure 2 gives an example of the variations measured in the EW and in the centroid velocity, for three subsequent nights in April 1996.

The EW shows peak-to-peak changes less than 10%. We can not decide whether the observed EW variation is the result of errors in the normalization of the spectra, or that it is intrinsic variation of ϵ Cen. The correlation diagram of the EW variations of both lines (Fig. 3) does not indicate that the EW variations of the λ 4552 Å and λ 4567 Å lines are related. The two lines are of the same triplet, so that intrinsic EW variations of both lines should, in principle, be correlated. The blends present in the triplet lines might be responsible for the observed difference in the EW variation of the two lines.

The velocity moments from the λ 4552 Å and λ 4567 Å lines show a very similar behavior, and their variations are correlated. The most striking variations are those of the centroid velocity, shown in Fig. 2. On the first shown night in that figure the variations of the centroid are minimal whereas on the third shown night a clear amplitude modulated signal is visible, with a maximum peak-to-peak variation of about 8 km s^{-1}. As only low-degree modes can cause such large variations in radial velocity, we derive that two or more low-degree modes should be present to cause the observed beating. These low-degree modes may also be responsible for the periodic photometric variations of the star (Shobbrook 1972; Heynderickx 1991, 1992). We analyse the variations of the velocity moments in Sect. 3.

We do not find clear traces of a possible orbit in our centroid-velocity measurements. The rapid centroid variations detected in all individual observing runs are centered around 10.4 km s^{-1}, for rest wavelength 4567.8 Å. If such an orbit exists, the related centroid variation during our observations must be less than ~5 km s^{-1}, i.e. smaller than the projected slit width.

3. Fourier analysis
3.1. Velocity moments

We have done a Fourier analysis of the equivalent width and moment variations of our spectra of ϵ Cen. We computed the
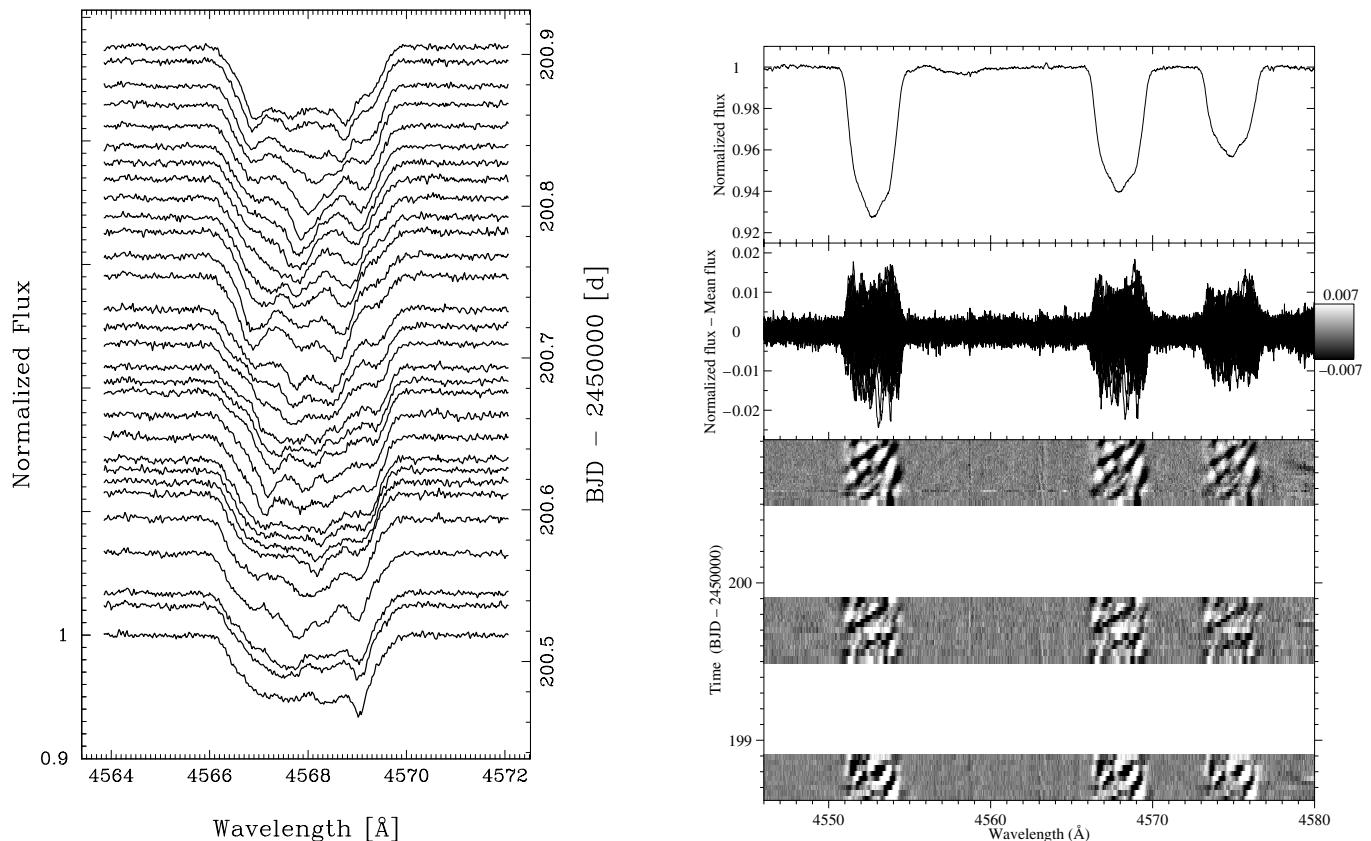
Fig. 1. *Left:* one night of data from April 1996, showing the variation in the SiIII λ 4567 Å line profile. The left vertical scale indicates normalized intensity. The spectra are offset according to their acquisition times. The continuum level of each spectrum indicates its acquisition time on the right vertical scale. *Right:* three subsequent nights of data from April 1996. *Top:* mean of 53 spectra. Note that the line profiles are not symmetric, which indicates that the beat periods of the pulsation modes are not properly sampled. *Middle:* residual spectra (mean subtracted). *Bottom:* grey scale representation of the residuals. Spectra are offset according to acquisition time.

Fourier components for frequencies between 0 and 30 d^{-1}, with a frequency spacing of 0.001 d^{-1}. Then we CLEANed the resulting Fourier spectrum in order to remove the temporal window function (which is due to incomplete sampling of the variational signal). We used CLEAN parameters $N_{\text{iterations}} = 400$ and a gain of 0.2 (Roberts et al. 1987). The *HWHM* of the main peak of the window function, which is 0.0005 d^{-1}, provides a first estimate for the errors of the measured frequencies. We elaborate on a more realistic error estimate in Sect. 4.5.

The resulting power spectra are displayed in Fig. 4. The most significant power peaks show up in the periodograms of the first and second velocity moments, displayed in the middle two panels of Fig. 4. The main frequencies are listed in Table 2. The equivalent width (*EW*) does not show much variation at these frequencies. This may indicate that the equilibrium T_{eff} of the star corresponds to that of the peak in the *EW* versus T_{eff} curve of the SiIII triplet such that temperature changes hardly give rise to changes in *EW*, implying a value of T_{eff} close to that derived by Code et al. (1976).

The strongest frequencies found in the variations of the centroid velocity, around 5.7 and 5.9 d^{-1}, agree with those found in photometric data by Shobbrook (1972). In the periodogram of the second and third moment we again find a peak at 5.9 c d^{-1} and an additional peak close to 6.2 c d^{-1}. The latter might be

Table 2. Strongest power peaks in the CLEANed Fourier spectra of the variations in the velocity moments of the 4567 Å line (see Fig. 4). The power peaks are ordered by their strength. Frequencies are given in d^{-1}.

	Centroid velocity	2nd velocity moment	3rd velocity moment
1	5.689	6.183	7.545
2	5.911	5.911	6.183
3	5.880	5.893	5.909
4	1.549		7.378

a one-day alias of the secondary peak found by Heynderickx (1991, 1992) in his Walraven photometry.

3.2. Line profile variations

We computed the residuals of the line profiles of each observing run by subtracting the mean profile for that particular run. To obtain residuals for the 16 spectra taken between runs, we used the mean profile of all spectra. The use of these residuals partly corrects for minute differences in the average *EW* and line depth between different observing runs, caused by small changes of the continuum and the vignetting of the light beam.
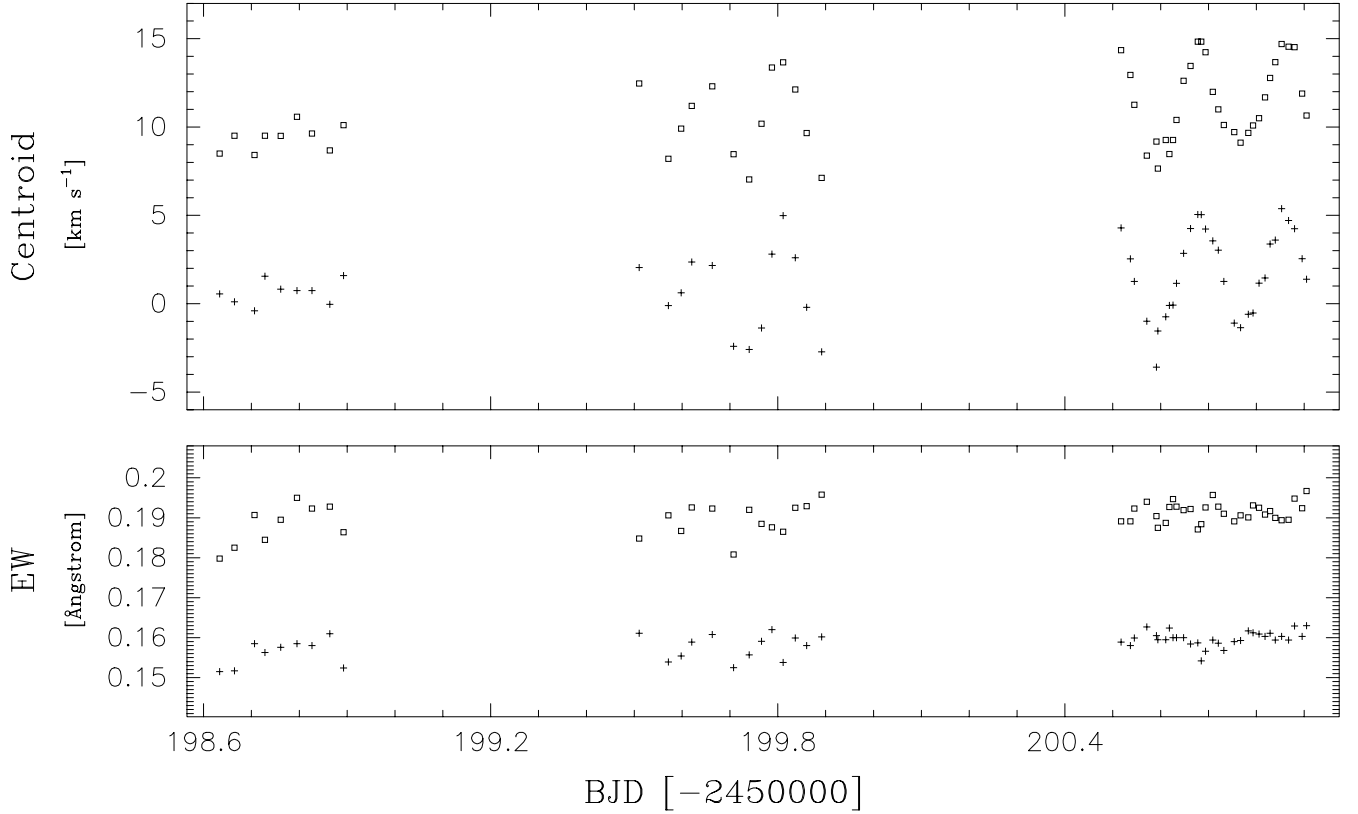
**Fig. 2.** Example of the equivalent width (*bottom panel*) and radial velocity (*top panel*) variations as measured from the $\lambda\,4567$ Å (open squares) and $\lambda\,4552$ Å (plus symbols) line profiles, for three consecutive nights in April 1996. The radial velocity variation displays long-term changes related to beating. The displayed nights are the same as in Fig. 1.
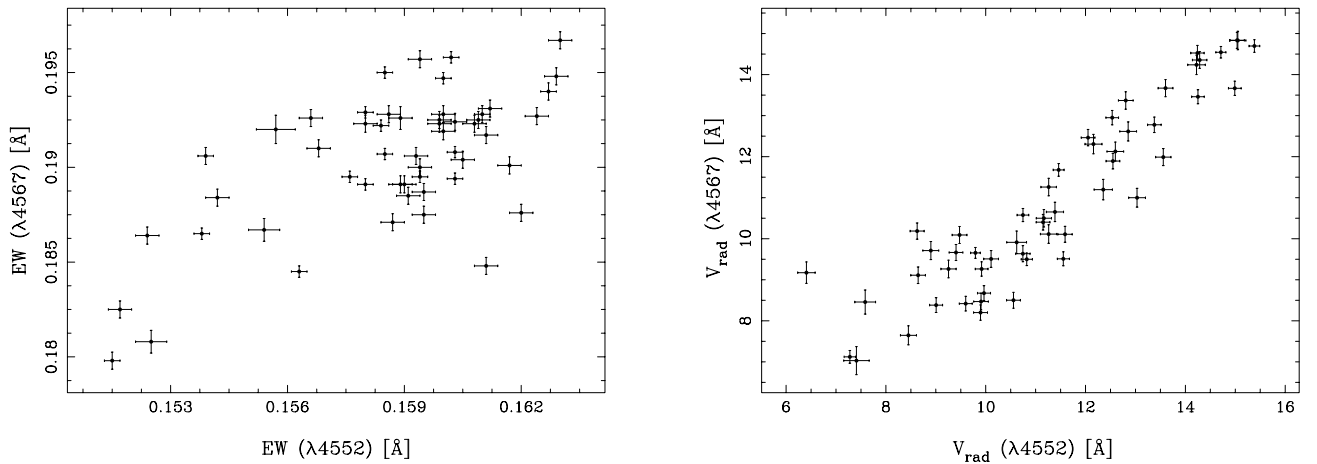
Fig. 3. *Left:* correlation diagram of the equivalent widths of the $\lambda\,4552$ Å and $\lambda\,4567$ Å line profiles, for the same three nights as in Fig. 2. The error bars indicate the statistical errors as measured from the S/N close to the concerned line profile; these do not include errors that arise from the reduction of the specta. *Right:* similar correlation diagram for the centroid variations in both lines. The relation between the centroid variations of the two lines is clearly visible.

To find the frequencies of the line-profile variations we use the analysis introduced by Gies & Kullavanijaya (1988), a method that we call the Intensity Period Search (IPS, see also S97). For each wavelength bin in the line profiles we perform a Fourier analysis of the variable signal. We used the same frequency domain and spacing and the same CLEAN parameters as with the velocity moments in Sect. 3.1.

For the Si III $\lambda\,4567$ Å line the result is plotted in Fig. 5. In this figure we see that the two-dimensional periodogram contains many local patches of variational power. Only at a few frequencies (most notably 7.645, 7.378, 6.183, 5.880 and 5.689 d^{-1}) we find power that is consistently present at different positions in the line profile. It is difficult to distinguish the true pulsation frequencies from the "false" frequencies, based only
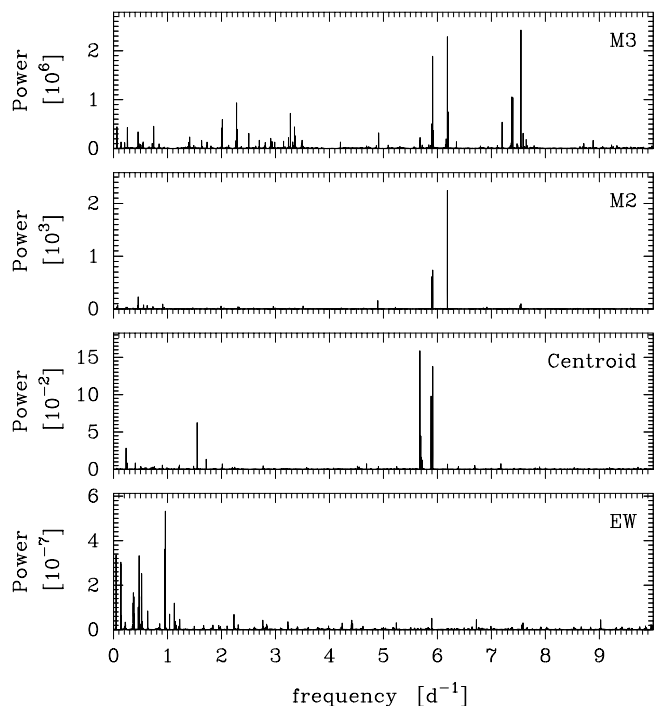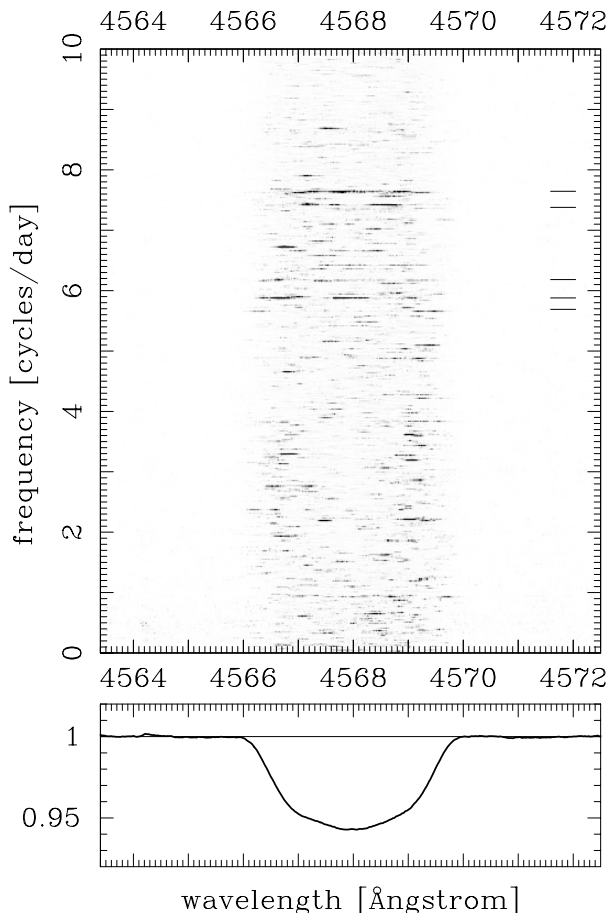
Fig. 4. Power spectra of the variation in *EW*, and the velocity moments M_1, M_2, and M_3. Table 2 lists the frequencies corresponding to the strongest peaks in these CLEANed Fourier spectra. See Sect. 3.1 for a description of the analysis


Fig. 5. *Top:* CLEANed Fourier analysis. For every wavelength bin (horizontal axis) a Fourier analysis of all spectra has been applied. The power resulting from the Fourier analysis is coded as a grey-value as a function of temporal frequency (vertical axis). Grey-scale cuts: $0-3 \times 10^{-7}$. *Bottom:* mean of all 530 spectra.

on the presence of power across the complete line profile. This is due to the CLEAN algorithm which is known to remove not only the power at alias-frequencies but at the true frequency as well (see e.g. similar analyses of ν Cen in Schrijvers & Telting 2002 and β Lupi in Schrijvers 1999). A better method to obtain the distribution of power across the line-profile is the use of multiple-sinusoid fits (see Sect. 4.1.2). We primarily use the Fourier analysis technique and CLEAN to obtain the frequency spectrum of ϵ Cen.

We performed a similar Fourier analysis for the data from the 4 individual observing runs as well. The periodograms from these datasets (not shown) show a lot of variational signal but in most cases the sampling does not suffice to resolve the underlying frequency pattern. Besides a frequency resolution which is too low for these datasets, the analyses suffer from one-day aliasing effects which can not be succesfully removed by the CLEAN algorithm.

The top panel of Fig. 6 shows the one-dimensional periodogram that results from summing the variational amplitudes of the two-dimensional periodogram over the line profile (4565.6–4570.3 Å). For comparison, we display the summed periodograms of the four individual observing runs in Fig. 7. It could be advocated that the analysis of the complete dataset gives a much clearer picture of the variations, and that the differences in the power spectrum from year to year are due mainly to the limitations of the time sequence and S/N in each run. The power spectra of the two runs in 1998 are very similar, which could be explained by the higher quality (in terms of

time span) of these two runs, but we can not exclude a longer term evolution of the actual pulsation spectrum.

The summed IPS periodogram in the top panel of Fig. 6 shows several peaks between 2 and 9 d^{-1}. We find again the two frequencies of Shobbrook (1972), and also one at 6.183 d^{-1} which we found in two of the velocity moments as well (M_2 and M_3). However, these three peaks are amongst the weaker features in the summed periodogram. We find two much stronger peaks at 7.645 and 7.378 d^{-1}. All significant peaks in the summed periodogram are indicated by the dotted lines in Fig. 6.

For two of the significant peaks (at 6.391 and 4.906 d^{-1}) we reject the possibility that these are directly related to pulsation modes, since we can identify these as one-day aliases of much stronger peaks in the power spectrum. The two one-day aliases show that the CLEAN algorithm, although reasonably succesful, was not able to remove one-day aliasing effects completely. Apart from these two one-day aliases there remain eight significant frequencies to be investigated: 2.233, 3.591, 3.801, 5.689, 5.880, 6.183, 7.378, and 7.645 d^{-1}. We investigate the characteristics of the variability at these eight selected frequencies in the next section.
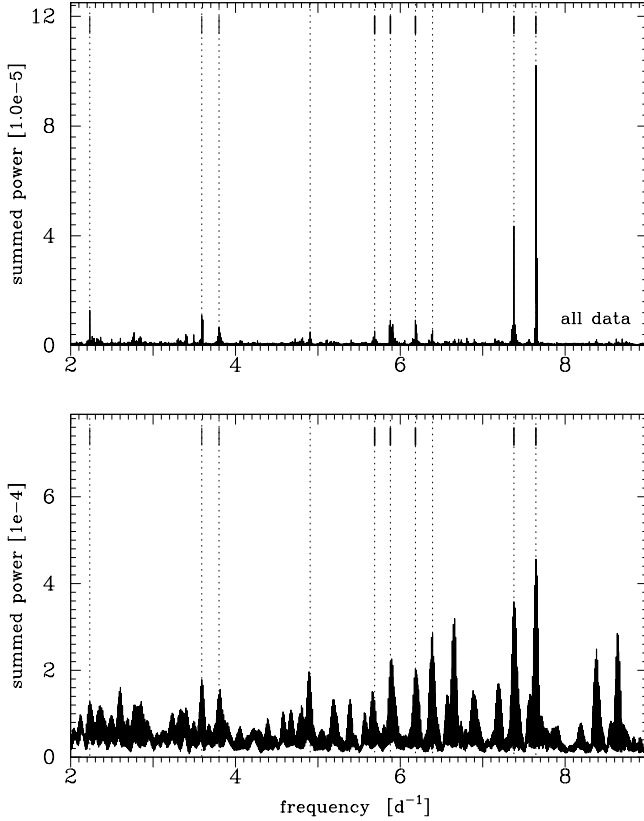
Fig. 6. *Top:* summed Fourier spectrum of all data. The power of the CLEANed periodogram of the λ 4567 Å line (Fig. 5) has been summed over the line profile. The vertical dotted lines indicate the frequencies with significant power. The solid lines at the top of the figures indicate the candidate frequencies of our pulsation mode analysis (see Sect. 4). Thick solid lines indicate frequencies succesfully identified as pulsation mode (see Sects. 4 and 5). *Bottom:* similar to top panel, but for the unCLEANed Fourier transform. The wide peaks in this diagram consist of many narrow peaks caused by aliasing effects (see Sect. 4.5).

Note that we verified that the frequency spectrum from our Fourier analysis is sufficiently resolved. For that purpose we performed a second calculation using 600 000 frequency bins between 0 and 30 d^{-1}. From the fact that both calculations lead to consistent results we conclude that a frequency spacing of 0.001 d^{-1} is sufficient for this dataset.

4. IPS amplitude and phase diagrams

4.1. IPS method

In S97 we defined a diagnostic tool for the analysis of non-radial pulsations in rotating stars. The method is based on the IPS (Intensity Period Search) diagnostic which consists of two diagrams, the amplitude and the phase diagram, giving a full representation of the line-profile variations caused by each of the individual pulsation modes.

The two diagrams are each related to distinct properties of the pulsation mode. The amplitude diagram contains information on mode parameters like the ratio of the horizontal to the vertical pulsation amplitude, k, the inclination of the star, i, the 3D velocity amplitude, V_{max}, the relative rotation rate, $\Omega/\omega^{(0)}$,
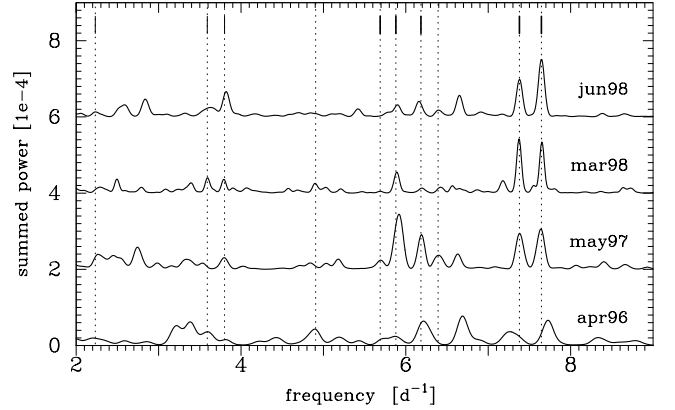
Fig. 7. Similar to Fig. 6. This figure shows the CLEANed periodograms of the data of the four individual observing runs. A frequency spacing of 0.01 d^{-1} was used for the Fourier transform, which is sufficient to resolve the frequency spectrum for these runs. As a reference, the same dotted lines as in Fig. 6 are shown.

the width of the intrinsic line profile, W, the amplitude of the temperature variation, $(\delta T/T)_{\mathrm{max}}$, the response of the EW to temperature changes, $\alpha_{W_{\mathrm{E}}}$ and the non-adiabatic phase lag of the temperature variation, χ^{na} (see S97 and Schrijvers & Telting 1999 for a thorough description of these parameters). The phase diagram is representative of the pulsation index ℓ (and $|m|$ if a harmonic is measured too). Telting & Schrijvers (1997, hereafter TS97) established a unique relation between the measured phase diagram and the ℓ-value of the responsible pulsation mode.

Here, we use two different techniques to calculate IPS diagnostics for each of the suspected pulsation frequencies. We will use these in Sect. 5 to determine the corresponding ℓ-values.

4.1.1. IPS diagrams from the Fourier transform

We use the Fourier transforms from Sect. 3 to investigate the amplitude and phase behavior across the line profile. For each of the candidate frequencies we plot the amplitudes and phases at each position in the line profile.

Some of the IPS amplitude diagrams obtained from the Fourier transform appear non-continuous and some of the IPS phase diagrams show discrete jumps, which might hamper further analysis. We therefore adopt a alternative method to create IPS diagnostics.

4.1.2. IPS diagrams from the direct fit approach

We created IPS diagnostics by fitting sinusoids with fixed frequencies to the intensity variation at each position in the line profiles. The input frequencies were taken from the results of the Fourier analysis. The main advantage of this approach is that the resulting amplitude diagrams are more continuous and that, consequently, the phase diagrams are more monotonic. We performed fits of the function

$$I(\lambda, t) = \sum_{i=1}^{N} A_i(\lambda) \sin(f_i t + \Psi_i(\lambda)) \tag{1}$$

to the intensity variations, where $A_i(\lambda)$ and $\Psi_i(\lambda)$ are the free parameters in the fit. For f_i we used the combination of the selected frequencies from Sect. 3.2. The IPS diagnostics are created by plotting $A_i(\lambda)$ and $\Psi_i(\lambda)$ across the line profile.

4.2. IPS application

For the eight selected frequencies (see Sect. 3.2) we compute IPS diagrams in two different ways. A first set of IPS diagnostics is constructed from the power and amplitude information from the CLEANed Fourier transform (indicated by the diagrams drawn with thin lines in Figs. 8 and 9). We applied a multiple-sinusoid fit (Eq. (1)) with f_i = (2.233, 3.592, 3.801, 5.689, 5.880, 6.183, 7.378, 7.645) to create a second set of amplitude and phase diagrams for each of the frequencies (thick lines in Figs. 8 and 9).

For three of the investigated frequencies (indicated by the thinner vertical lines in Fig. 6) we were not able to obtain IPS diagnostics that are in any way similar to those generated with theoretical models of non-radial pulsations. We cannot decide whether these frequencies are caused by pulsations or by other effects or phenomena.

For five of the investigated frequencies (indicated by the thick vertical lines in Fig. 6) the line-profile variability is typical for non-radial pulsations. The diagnostic diagrams obtained at these frequencies are displayed in Figs. 8 and 9.

In each of the phase diagrams we measure the maximum phase differences $\Delta\Psi$, as the maximum blue-to-red phase difference found over the region in the line profile where we find significant amplitudes (See Fig. 2 of TS97 for instructive examples of how we measure $\Delta\Psi$ from the phase diagram). We will later use the value of $\Delta\Psi$ to determine an ℓ value for each frequency. We determined $\Delta\Psi$ for the IPS phase diagrams obtained with both methods, i.e. the Fourier transform and the multiple-sinusoid fit. These values for $\Delta\Psi$ are listed in Table 3.

4.3. Search for the typical IPS characteristics of non-radial pulsation modes

We performed a visual inspection of the variability at all frequencies between 0 d^{-1} and 10 d^{-1}. For this, we fitted single sinusoids to the signal at each wavelength bin, i.e. we used Eq. (1) with $N = 1$. We repeated the single-sinusoid fit for all frequencies f_i between 0 and 10 d^{-1}, with frequency steps of 0.001 d^{-1}. For each fit we constructed IPS amplitude and phase diagrams.

We visually inspected each of these diagrams for possible "finger prints" of non-radial pulsation modes in rotating stars. A typical IPS diagnostic satisfies at least two conditions. Firstly, significant amplitudes should be present in all wavelength bins in a region that extends at least between $-V_e \sin i$ and $+V_e \sin i$. A second condition is that the phase diagram is smooth, without jumps, and that it shows a gradual change between $-V_e \sin i$ and $+V_e \sin i$.

We find IPS diagrams that fulfil these two requirements at frequencies close to the five frequencies in Table 3, and within the domains specified by the errors (see Sect. 4.5) of those frequencies. The IPS diagnostics derived for the main peaks and their side peaks are very similar. We also find pulsation-compatible IPS diagnostics at the two one-day alias frequencies mentioned in Sect. 3.2. At all other frequencies the diagnostics are not compatible with non-radial pulsation models.

These findings ensure that we did not overlook possible other pulsation modes responsible for some of the smaller peaks in the frequency spectrum.

4.4. Folding of spectra

We apply a technique of folding the spectra, which is similar to the folding techniques often seen in photometric studies of variable stars. The folding technique is repeated for each wavelength bin. For each spectrum we take the modulus of the acquisition time and the considered period, P_i. We then apply a temporal re-sampling of the spectra to only eight spectra between time $t = 0$ and $t = P_i$. Each of the eight resulting spectra is created by averaging all spectra in time-bins of width $P_i/8$. Using eight spectra is a useful compromise because this samples the considered period well enough to resolve the characteristics of the related line-profile variations, while keeping the number of averaged spectra high enough to average out most variability at the other periods. This technique enables to visualize the line-profile variations related to each individual pulsation period. For each of the five frequencies in Table 3 we show the folded spectra in the top panels of Figs. 8 and 9.

4.5. Accuracy of the frequency determinations

As mentioned before, the $HWHM$ of the main peak of the window function provides a first estimate for the errors on the obtained frequencies. Although the peaks in the summed periodogram are accordingly narrow, a close inspection of the main peaks learns that each peak is on both sides accompanied by smaller peaks (see Fig. 10), separated from the main peak by sums of 0.013 d^{-1}, and to a lesser degree also 1.016 d^{-1}, i.e. we find side peaks at $f = f_{\text{main}} \pm \Delta f$, where $\Delta f \in \{0.013, 0.016, 0.026, 0.029\}$. We observe a very similar pattern around the main peak of the window function, which indicates that the additional frequencies are related to sampling issues rather than to a real phenomenon. We prewhitened the data with each of the investigated frequencies and in all cases the smaller peaks disappear together with the main power peak. This again indicates that each main peak and its smaller side peaks are the result of only one source of variability.

We created IPS diagnostics for the strongest side peaks, like those presented in Figs. 8 and 9. Many of the side peaks give similar results for $\Delta\Psi$, whereas others give rise to useless IPS diagnostics.

It could well be that the small peaks on both sides of the main peak are the result of aliasing effects caused by the gaps between our observing runs. For example, the gap between our last observations from March 1998 and the first observations from June 1998 is approximately 63 days, which nicely fits the side peaks at distances of 0.016 d^{-1} to the main peaks.
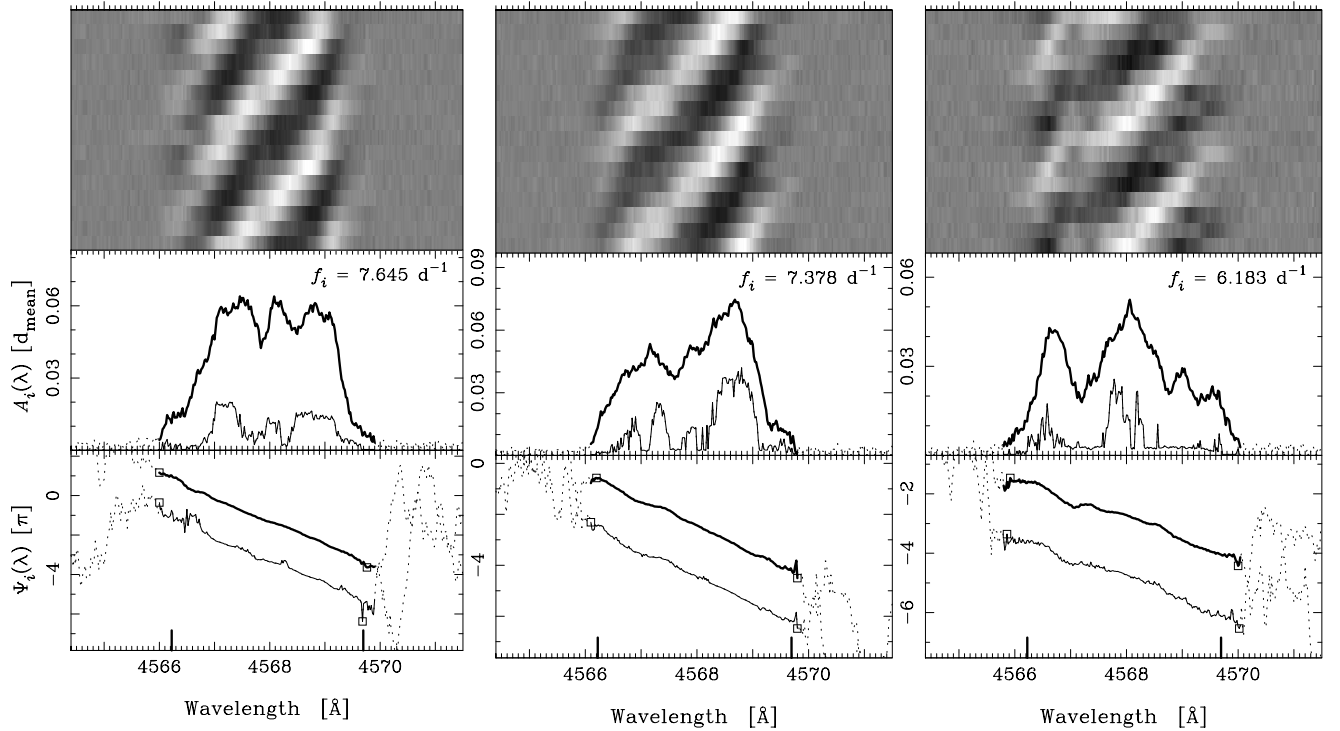
Fig. 8. *Top* (gray coded): residuals (mean of all spectra is subtracted) of the folded spectra, displayed over 2 pulsation periods. *Bottom* (two graphs): diagnostics for the variations found in the $\lambda\,4567$ Å line-profile at frequencies 7.645, 7.378 and 6.183 d^{-1}. Each diagnostic consists of two diagrams: the top diagram displays the amplitude distribution $A_i(\lambda)$ and the bottom diagram shows the phase distribution $\Psi_i(\lambda)$, as a function of wavelength λ. The wavelengths corresponding to $-V_e \sin i$ and $+V_e \sin i$ ($V_e \sin i = 114\,\mathrm{km\,s^{-1}}$, from Brown & Verschueren 1997) are marked on the bottom axis. The amplitudes are in units of d_mean, which is the central absorption depth of the mean line-profile. For the $\lambda\,4567$ Å line we find $d_\mathrm{mean} = 0.05718$ in continuum units. For the region with significant amplitude the diagrams are drawn with a solid line. Outside this region a dotted line is used. The positions of the phase diagram at which we measure $\Delta\Psi_i$ are indicated by a square symbol. The IPS diagrams resulting from the multiple-sinusoid fit are drawn as a heavy line, whereas a thin line is used for the IPS diagnostics from the CLEANed Fourier transform.
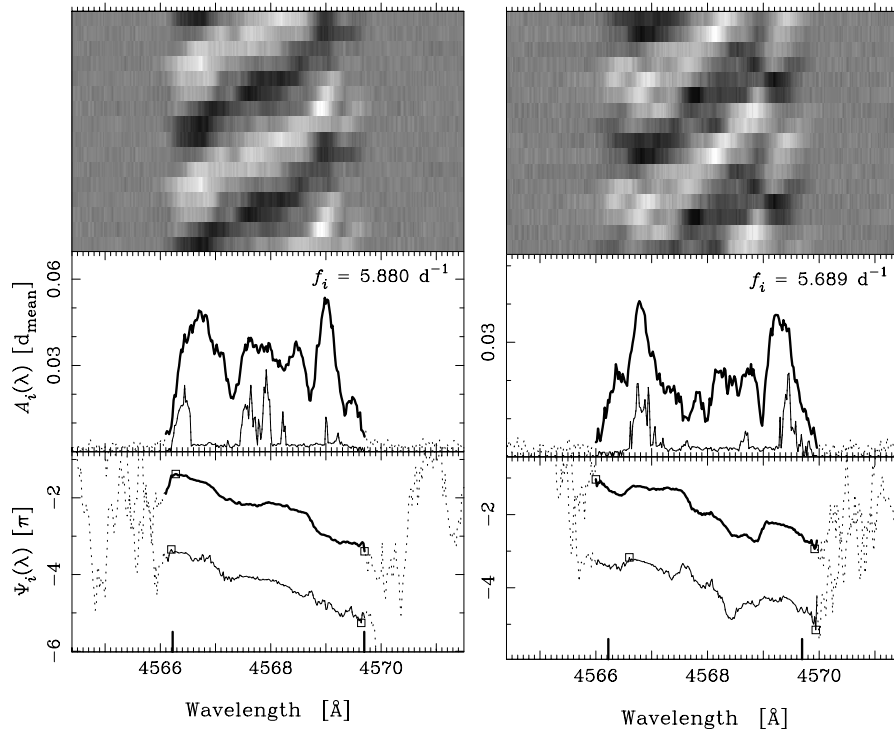
Fig. 9. Similar to Fig. 8, but for the frequencies 5.645 and 5.880 d^{-1}.

Table 3. Mode identification. The frequencies found in the summed Fourier transforms of the Si III $\lambda\,4567$ Å line profile. Only the frequencies for which our mode-identification was successful are listed here; for the investigated frequencies of 2.233, 3.591 and 3.801 d^{-1} we could not obtain useful IPS diagrams. The first column lists the frequency and the second gives the corresponding error (see Sect. 4.5). Column 3 gives the periods. The maximum blue-to-red phase differences $\Delta\Psi_i$ measured from the IPS diagnostics calculated from the Fourier transform (label FT) and the multiple-sinusoid fit (label MF) are in Cols. 5 and 6. Columns 7–10 list the fractional ℓ values calculated from Col. 6 by means of Eq. (2). The rightmost column lists the value for ℓ from our finally adopted interpretation of the diagnostics.

f_{obs} [d^{-1}]	Error [d^{-1}]	P_{obs} [h]	Also in moments	$\Delta\Psi_i^{FT}$ [π]	$\Delta\Psi_i^{MF}$ [π]	ℓ ($\ell-\|m\|<6$)	ℓ ($k^{(0)}<0.3$)	ℓ ($k^{(0)}>0.7$)	ℓ ($\|m\|>2$)	ℓ
5.689	±0.032	4.219	M_1	1.99	1.90	2.12	1.99	2.25	–	2
5.880	±0.032	4.082	$M_1\ M_2\ M_3$	1.91	2.01	2.24	2.11	2.37	–	2
6.183	±0.032	3.882	$M_2\ M_3$	3.18	2.96	3.30	3.16	–	3.43	3
7.378	±0.029	3.253	M_3	4.17	3.93	4.37	4.23	–	4.48	4
7.645	±0.013	3.139		6.03	4.81	5.34	5.19	–	5.43	5

We can not rule out that the actual pulsation frequency (in the observer's frame) is at one of the smaller peaks instead of the main peak. We therefore use the side peaks to determine more appropriate error estimates for the investigated frequencies. These error estimates are determined by the width of the region around the main peak, in which we find side peaks exceeding the noise level. Since the number of side peaks differs for each of the investigated frequencies, this leads to different error estimates. The error estimates are listed in Table 3.

5. Mode identification

To relate the measured values for the maximum blue-to-red phase difference, $\Delta\Psi$, to the degree ℓ of the responsible non-radial pulsation modes, we use Eq. (8) of TS97:

$$\ell = p_\ell + q_\ell |\Delta\Psi|/\pi. \tag{2}$$

For the present analysis we chose to compare four combinations for (p_ℓ, q_ℓ) from Table 2 of TS97 (see our Table 4). The different combinations of (p_ℓ, q_ℓ) apply to different subsets of parameter space.

In the following sections, our determination of the ℓ values from the phase diagrams is addressed for each of the frequencies. The ℓ-values derived for each of the (p_ℓ, q_ℓ) combinations are listed in Table 3, together with our final ℓ-determination.

In relation to the derived ℓ-values the implications for a prograde or a retrograde character of the pulsation modes are discussed. The observed blue-to-red movement of the bumps across the line-profile could in principle be caused by both prograde and retrograde modes, but for the latter (retrograde mode, blue-to-red movement of the bumps) the following restriction exists:

$$\omega_{obs} < m\Omega \tag{3}$$

where $m > 0$ and $\omega_{obs} = 2\pi f_{obs}$ (see Eq. (4) in TS97). For a given m, this condition provides a lower limit for the star's rotation rate Ω which may be used to reject the possibility of a retrograde mode. Such rejections turn out to be possible for all 5 frequencies f_{obs} from Table 3, as shown below.
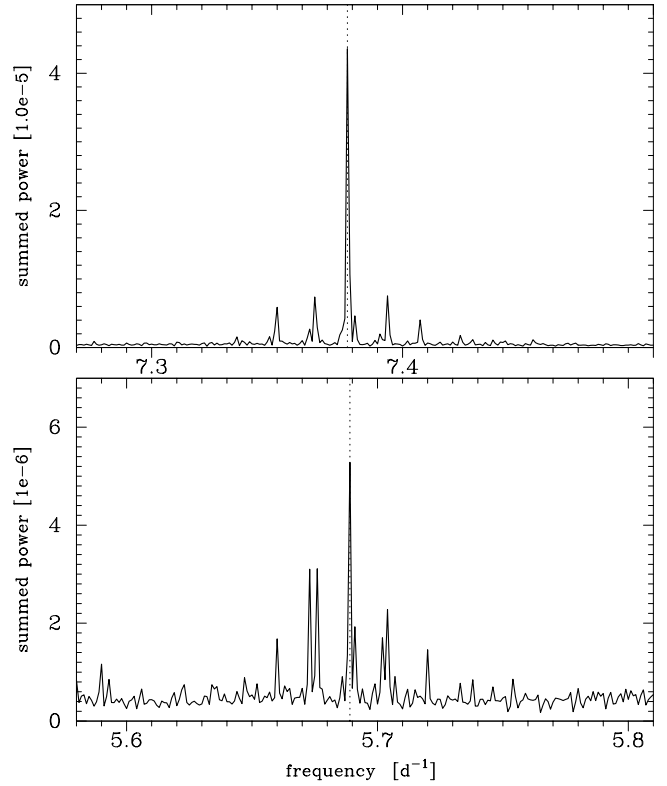
Fig. 10. Similar to Fig. 6. This figure displays the summed periodogram from the CLEANed Fourier transform, but zoomed into the small regions around 7.378 and 5.689 d^{-1}, illustrating the side peaks. The two plots also show the difference in relative magnitude of the smaller peaks: around 7.378 d^{-1} the side peaks are relatively small whereas the relative strength of the side peaks around 5.689 d^{-1} is much larger. We cannot rule out that in some cases the actual pulsation frequency is at one of the smaller peaks instead of the main peak.

5.1. Variability at $f = 7.645$, $f = 7.378$ and $f = 6.183$ d^{-1}

The characteristics of the line-profile variability found at $f = 7.645$, $f = 7.378$ and $f = 6.183$ d^{-1}, i.e. the IPS phase and amplitude diagrams for these frequencies, agree closely to what is expected for non-radial pulsations (see Fig. 8). The amplitude diagrams show variability across the complete line profile, and

Table 4. Combinations (p_ℓ, q_ℓ), applying to different subsets of parameter space (From TS97).

Condition	p_ℓ	q_ℓ	Prob [$\ell-1$, $\ell+1$]
General	0.099	1.090	71%
$\ell-\|m\| < 6$	0.015	1.109	84%
$k^{(0)} < 0.3$	-0.098	1.100	94%
$k^{(0)} > 0.7$	0.188	1.087	67%
$\|m\| > 2$	0.226	1.082	80%

the phase diagrams are smooth and well-determined. Applying Eq. (2) to the measured values of $\Delta\Psi$, we find that $\ell = 5$, $\ell = 4$ and $\ell = 3$ are the best solutions for these modes.

The condition for retrograde modes in Eq. (3) leads to lower limits on Ω for each of the modes. For retrograde modes the lower limits on the rotation rate would be $\Omega > 1.529$ d^{-1}, $\Omega > 1.845$ d^{-1} and $\Omega > 2.061$ d^{-1}, respectively. We regard such values for the rotation rate too large for ϵ Cen. These three pulsation modes must therefore be prograde.

5.2. Variability at f = 5.880 and f = 5.689 d^{-1}

The characteristics of the variability measured at 5.880 and 5.689 d^{-1} turn out to be similar (see Fig. 9). Most importantly, the measured blue-to-red phase differences $\Delta\Psi$ at these two frequencies do not differ much (see Table 3). This of course means that if we strictly apply the statistical relations of TS97 (Eq. (2) and Table 4) we find the same value of $\ell = 2$ for both modes. However, the linear relations between $\Delta\Psi$ and ℓ as determined by TS97 must be used with care when it concerns $\Delta\Psi \lesssim 2\pi$. Their Fig. 9 shows that for values of $\Delta\Psi$ between $\sim\pi$ and $\sim 2\pi$, pulsation modes with either $\ell = 0$ or $\ell = 2$ are likely to be responsible, and to a lesser degree also $\ell = 1$. For both of the two frequencies we can exclude the possibility of $\ell = 0$; Heynderickx (1991) already pointed out that the photometric amplitudes at different wavelengths are not compatible with radial modes. Figure 9 of TS97 also shows that the ratio of the horizontal to the vertical amplitude, k, might allow to discriminate between $\ell = 1$ and $\ell = 2$. Although $\ell = 2$ is the preferred solution for $\Delta\Psi \approx 2\pi$ regardless of k, a known value of $k > 0.7$ would exclude $\ell = 1$.

Another similarity between the IPS diagnostics for $f = 5.880$ and $f = 5.689$ d^{-1} is that in both cases the amplitude distribution across the line profile appears double-peaked, which is a well known indication of a high k-value. However, S97 pointed out that double-peaked amplitude distributions do not unambiguously imply a high k-value if $\Delta\Psi \lesssim 2\pi$. This means that the amplitude diagrams at $f = 5.880$ and $f = 5.689$ d^{-1} can not be used to constrain k.

Although we find significant amplitudes across the line-profile, the phase diagrams of the variability at these two frequencies turn out to be only marginally compatible with phase diagrams from non-radial pulsation modes. Especially the phase diagram at $f = 5.689$ d^{-1} shows steep changes which are not known from modelled line-profile variations. More observations are needed to confirm or reject these frequencies as related to pulsation modes.

We tentatively conclude $\ell = 2$ for both $f = 5.880$ and $f = 5.689$ d^{-1}. Assuming that these frequencies are related to retrograde pulsation modes, the lower limits on the rotation rate provided by Eq. (3) would be $\Omega > 2.940$ d^{-1} and $\Omega > 2.845$ d^{-1}, respectively. Again, we regard such values for the rotation rate too large for ϵ Cen. The option of retrograde modes is therefore also excluded for these two frequencies. If caused by pulsation, the modes behind these two frequencies must be prograde.

6. Concluding remarks

As advocated by Jerzykiewicz (1994) the β Cephei star ϵ Cen provides an excellent opportunity to do asteroseismology: the star is multi-periodic and many of its fundamental parameters are known.

We have obtained and analyzed a set of 530 spectra of ϵ Cen. We found the absorption lines of the SiIII triplet to be variable.

We Fourier analyzed the intensity variations at each position in the line-profiles, as well as the variations of the first three velocity moments. The detected intensity variations provide evidence for three prograde high-degree non-radial pulsation modes. We identify these as $\ell = 5$, $\ell = 4$ and $\ell = 3$.

At two other frequencies, which were already known from published photometric studies of ϵ Cen, we also find intensity variations across the line profiles. These two frequencies dominate the radial-velocity variation as well. The line-profile variations detected at these two frequencies are only marginally consistent with what is expected for non-radial pulsation modes. We tentatively conclude that two prograde non-radial pulsation modes with $\ell = 2$ are responsible for these frequencies.

We have shown that high-resolution spectroscopy may reveal many pulsation modes if enough data is acquired over a sufficiently long time base.

This work shows dramatically that high-resolution spectroscopy allows us to obtain information about the pulsational behavior of rotating stars, that can not be obtained with photometric techniques. The high-degree modes detected in ϵ Cen could not be retrieved from photometry because the amplitudes of the related light variations are too small. We emphasize the importance of high-resolution spectroscopy for the asteroseismological research of pulsating stars. Without this technique a large portion of the vibrational properties of these stars remains unknown.

Determination of the exact pulsation frequencies is crucial for asteroseismological applications, as well as a solid identification of both ℓ and m. This work shows that, in the case of ϵ Cen, the application of true asteroseismology requires an even more extensive data set than the one presented, in order to precisely pin down the pulsation frequencies and modal parameters. More advanced mode identification algorithms that utilize model fitting techniques might then be required for improvements on mode identification.

ceasing support and advice. We thank Douglas Gies for his improvements to the manuscript.

References

Aerts, C., De Pauw, M., & Waelkens, C. 1992, A&A, 266, 294

Balona, L. A., & Shobbrook, R. R. 1984, MNRAS, 211, 375

Balona, L. A. 1986, MNRAS, 219, 111

Blaauw A. 1964, ARA&A, 2, 213

Brown, A. G. A., & Verschueren W. 1997, A&A, 319, 811

Code, A., Bless, R. C., Davis, J., & Brown, R. H. 1976, ApJ, 203, 417

De Geus, E. J., De Zeeuw, P. T., & Lub. J. 1989, A&A, 216, 44

De Zeeuw, P. T, Hoogewerf, R., De Bruijne, J. H. J., Brown, A. G. A., & Blaauw, A. 1999, AJ, 117, 354

Gies, D. R., & Kullavanijaya, A. 1988, ApJ, 326, 813

Hanbury, Brown, R. 1974, The intensity interferometer. Its applications to astronomy (London: Taylor & Francis)

Heynderickx, D. 1991, Ph.D. Thesis, K. U. Leuven

Heynderickx, D. 1992, A&AS, 96, 207

Heynderickx, D., Waelkens, C., & Smeyers, P. 1994, A&AS, 105, 447

Hoffleit, D., & Jaschek, C. 1982, The Bright Star Catalogue, Yale University Observatory, electronic version 5

Jerzykiewicz, M. 1994, in Pulsation, rotation and mass loss in early-type stars, ed. L. A. Balona, H. F. Henrichs, & J. M. Le Contel (Dordrecht: Kluwer Academic Publisher), 3

North, P., & Nicolet, B. 1990, A&A, 228, 78

Roberts, D. H., & Lehár, J., Dreher, J. W. 1987, AJ, 93, 968

Schrijvers, C., Telting, J. H., Aerts, C., Ruymaekers, E., & Henrichs, H. F. 1997, A&AS, 121, 343 (S97)

Schrijvers, C. 1999, Ph.D. Thesis

Schrijvers, C., & Telting, J. H. 1999, A&A, 342, 453

Schrijvers, C., & Telting, J. H. 2002, A&A, 394, 603

Shobbrook, R. R. 1972, MNRAS, 157, 5

Telting, J. H., & Schrijvers, C. 1997, A&A, 317, 723 (TS97)

Telting, J. H., & Schrijvers, C. 1998, A&A, 339, 150